ADVANCES IN ATMOSPHERIC SCIENCES, VOL. 29, NO. 1, 2012, 118–134

Application of the Conditional Nonlinear Optimal Perturbation Method to the Predictability Study of the Kuroshio Large Meander

WANG Qiang[1,2,3] (王 强), MU Mu*[3,1] (穆 穆), and Henk A. DIJKSTRA[4]

[1]*State Key Laboratory of Numerical Modeling for Atmospheric Sciences and Geophysical Fluid Dynamics, Institute of Atomspheric Physics, Chinese Academy of Sciences, Beijing* 100029

[2]*Graduate University of the Chinese Academy of Sciences, Beijing* 100049

[3]*Key Laboratory of Ocean Circulation and Wave, Institute of Oceanology, Chinese Academy of Sciences, Qingdao* 266071

[4]*Institute for Marine and Atmospheric Research Utrecht, Department of Physics and Astronomy, Utrecht University,* 3584 *CC Utrecht, the Netherlands*

(Received 17 November 2010; revised 7 June 2011)

ABSTRACT

A reduced-gravity barotropic shallow-water model was used to simulate the Kuroshio path variations. The results show that the model was able to capture the essential features of these path variations. We used one simulation of the model as the reference state and investigated the effects of errors in model parameters on the prediction of the transition to the Kuroshio large meander (KLM) state using the conditional nonlinear optimal parameter perturbation (CNOP-P) method. Because of their relatively large uncertainties, three model parameters were considered: the interfacial friction coefficient, the wind-stress amplitude, and the lateral friction coefficient. We determined the CNOP-Ps optimized for each of these three parameters independently, and we optimized all three parameters simultaneously using the Spectral Projected Gradient 2 (SPG2) algorithm. Similarly, the impacts caused by errors in initial conditions were examined using the conditional nonlinear optimal initial perturbation (CNOP-I) method. Both the CNOP-I and CNOP-Ps can result in significant prediction errors of the KLM over a lead time of 240 days. But the prediction error caused by CNOP-I is greater than that caused by CNOP-P. The results of this study indicate not only that initial condition errors have greater effects on the prediction of the KLM than errors in model parameters but also that the latter cannot be ignored. Hence, to enhance the forecast skill of the KLM in this model, the initial conditions should first be improved, the model parameters should use the best possible estimates.

Key words: conditional nonlinear optimal perturbation, Kuroshio large meander, predictability, model parameters

Citation: Wang, Q., M. Mu, and H. A. Dijkstra, 2012: Application of the conditional nonlinear optimal perturbation method to the predictability study of the Kuroshio large meander. *Adv. Atmos. Sci.*, **29**(1), 118–134, doi: 10.1007/s00376-011-0199-0.

1. Introduction

The Kuroshio is the strong western boundary current of the North Pacific subtropical gyre. It transports a large amount of heat from the tropical to the subtropical regions. For this reason, the Kuroshio has a significant impact on the climate of the North Pacific (Latif and Barnett, 1994) and consequently on local fisheries and ship navigation.

Observation data have shown that the Kuroshio

*Corresponding author: MU Mu, mumu@qdio.ac.cn

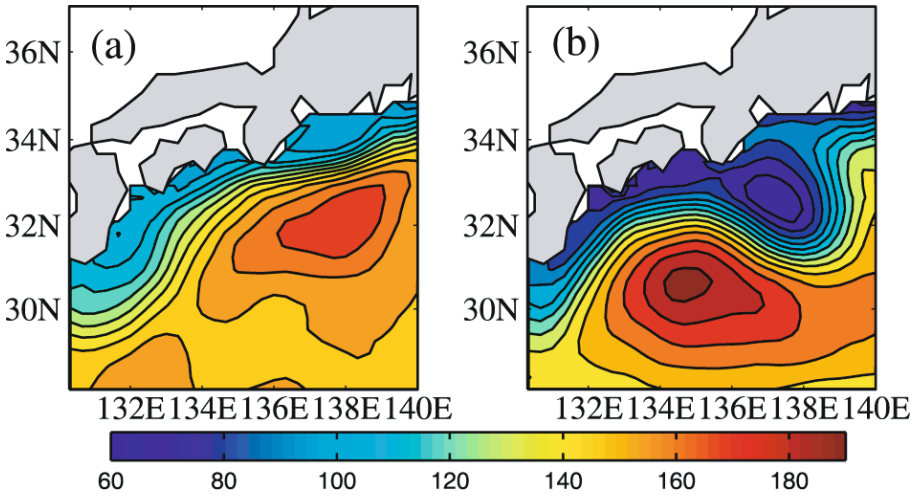

Fig. 1. Examples of the bimodal paths of the Kuroshio south of Japan. The mean sea surface height fields from AVISO for the period of (a) July 2003 to June 2004 and (b) July 2004 to June 2005 are plotted. Contour intervals are 10 cm. Units: cm.

path south of Japan exhibits typical bimodal features, namely, the nonlarge meander path (NLM) and the large meander path (KLM; Taft, 1972). Figure 1 shows the observational sea-surface height (SSH) patterns of the bimodal path of the Kuroshio as determined using satellite altimetry. This satellite SSH data was produced and distributed by Archiving, Validation and Interpretation of Satellite Oceanographic data (AVISO). The data, which are high resolution of $(1/3)^\circ \times (1/3)^\circ$ Mercator grid, are available at www.aviso.oceanobs.com. As shown in Fig. 1, the Kuroshio was in a NLM state in JUL 2003–JUN 2004 (Fig. 1a), while it was in a KLM state in JUL 2004–JUN 2005 (Fig. 1b). Long-term observations show that each path can persist from a few years to a decade. In contrast, the actual transition between the two typical paths can take place within several months (Kawabe, 1995).

Several numerical and observational studies about the transition between NLM and KLM have been performed (Masuda, 1982; Chao and McCreary, 1982; Kawabe, 1985; Yasuda et al., 1985; Akitomo et al., 1997; Qiu and Miao, 2000; Schmeits and Dijkstra, 2001; Waseda et al., 2002, 2003; Tsujino et al., 2006). The results of these studies have been used to understand the mechanism of the transition and to provide guidance for improving the numerical model. Recently, several researchers investigated the predictability of the Kuroshio path variations, especially the transition to the KLM state. Komori et al. (2003) conducted the short-range forecast experiments of the Kuroshio path variabilities using a 1.5-layer shallow-water model and a variational data assimilation scheme. They found the predictive limit for the KLM to be ∼60 days. Kamachi et al. (2004) performed the forecast experiments using an operational data assimilation scheme and prediction model. They suggested the predictive limit for the KLM to be ∼80 days. Usui et al. (2006) also conducted similar forecast experiments, but they used an eddy-resolving model and concluded the predictive limit to be from 40 to 60 days and to depend on the transition stages of the Kuroshio meander. Miyazawa et al. (2005) performed an ensemble forecast of the Kuroshio meander and concluded the predictive limit to be ∼80 days. In addition to estimating the predictive limit, Ishikawa et al. (2004) investigated the sensitivity of prediction results of the KLM to initial conditions using the adjoint method. They concluded that initial error has an important impact on prediction. In these studies, only the impacts of the initial error on prediction were discussed. However, prediction errors are generally caused by both initial and model errors. In a numerical forecast model, model error may also result in a substantial prediction error (Orrell, 2003).

An important aspect of model error is the amount of error in model parameters. Chu et al. (1999) studied the impact of uncertainty in a model parameter on prediction results by superimposing different perturbations on the model parameter. Similarly, Liu (2002) and Orrell (2003) investigated the influence of the uncertainty on each model parameter in a climate model. However, when multiple model parameters simultaneously have uncertainties, it is difficult to estimate the greatest impact on the prediction using a method in which different perturbations are applied to model parameters.

To overcome this difficulty, Mu et al. (2010) ex-

tended the conditional nonlinear optimal perturbation (CNOP) method previously proposed by Mu et al. (2003) to find the optimal mode of model parameter perturbations. The optimal parameter perturbation has been referred to as CNOP-P. Yu (2009) and Duan and Zhang (2010) studied the spring predictability barrier phenomenon for El Niño events using the CNOP-P approach and concluded that model parameter errors may not cause a significant spring predictability barrier for El Niño events.

In this study we used the CNOP-P approach to investigate the effects of the uncertainties of the model parameters on prediction of the KLM, ignoring other possible kinds of model errors. Simultaneously, the conditional nonlinear optimal initial perturbation (CNOP-I) method was used to examine the impacts of the uncertainties in initial conditions on the prediction of the KLM. We compared the prediction errors caused by CNOP-I error and CNOP-P errors, respectively, and evaluated which kind of errors had the greatest influence on the prediction of the KLM. In summary, given a dynamical model that exhibits reasonable instabilities of interest, the CNOP-P method was used to investigate the potential prediction error related to the model parameter uncertainties, in comparison with the imperfection of initial conditions.

The paper is organized as follows. In section 2, the CNOP-I and CNOP-P approaches are briefly reviewed. The numerical model adopted in this study is briefly presented in section 3. In section 4, the ability of the model to simulate the Kuroshio path variations is examined. The effects of initial condition errors and model parameter errors on the prediction of the KLM are investigated in section 5. Some discussion about the sensitivity of the results is presented in section 6. The conclusions are summarized in section 7.

2. CNOP-I and CNOP-P approaches

In this section, we introduce the CNOP-I and the CNOP-P methods.

The equations governing the evolution of the state vector $\boldsymbol{X}$ can be written as

$$\begin{cases} \dfrac{\partial \boldsymbol{X}}{\partial t} = \boldsymbol{F}(\boldsymbol{X}, \boldsymbol{p}) \,, \\ \boldsymbol{X}|_{t=0} = \boldsymbol{X}_0 \,, \end{cases} \tag{1}$$

where t indicates time, $\boldsymbol{X}_0$ is the initial condition, $\boldsymbol{p} = (p_1, p_2, \cdots, p_m)^{\mathrm{T}}$ denotes the model parameter vector, and $\boldsymbol{F}$ is a nonlinear differential operator. If the initial state $\boldsymbol{X}_0$ is known, the future state $\boldsymbol{X}(t)$ can be obtained by integrating Eq. (1). Hence, the solution to Eq. (1) can be formally written as

$$\boldsymbol{X}(t) = \boldsymbol{M}_t(\boldsymbol{p})(\boldsymbol{X}_0) \,, \tag{2}$$

where $\boldsymbol{M}_t(\boldsymbol{p})$ is the nonlinear propagator [it propagates the initial state $\boldsymbol{X}_0$ to the future state $\boldsymbol{X}(t)$] with the parameter vector $\boldsymbol{p}$.

Suppose there are two initial states $\boldsymbol{X}_0$ and $\boldsymbol{X}_0 + \boldsymbol{x}_0$. Then from Eq. (1), we obtain two solutions $\boldsymbol{X}(t)$ and $\boldsymbol{X}(t) + \boldsymbol{x}(t)$:

$$\boldsymbol{X}(t) = \boldsymbol{M}_t(\boldsymbol{p})(\boldsymbol{X}_0), \boldsymbol{X}(t) + \boldsymbol{x}(t) = \boldsymbol{M}_t(\boldsymbol{p})(\boldsymbol{X}_0 + \boldsymbol{x}_0) \,.$$

Hence when $\boldsymbol{x}_0$ is regarded as an initial perturbation on the time-dependent reference state $\boldsymbol{X}(t)$, $\boldsymbol{x}(t)$ denotes the nonlinear evolution of this initial perturbation.

A nonlinear constraint optimization problem is defined as

$$J(\boldsymbol{x}_0^*) = \max_{\boldsymbol{x}_0 \in C_\delta} J(\boldsymbol{x}_0) \,, \tag{3}$$

where $\boldsymbol{x}_0 \in C_\delta$ denotes the initial constraint condition and C_δ is closed, which often is defined as a ball with a chosen norm such as $C_\delta = \{\, \boldsymbol{x}_0 | \, \|\boldsymbol{x}_0\| \leqslant \delta \}$. $J(\boldsymbol{x}_0)$ is an objective function defined as follows:

$$J(\boldsymbol{x}_0) = \frac{1}{2} \left\| \boldsymbol{M}_t(\boldsymbol{p})(\boldsymbol{X}_0 + \boldsymbol{x}_0) - \boldsymbol{M}_t(\boldsymbol{p})(\boldsymbol{X}_0) \right\|^2 \,. \tag{4}$$

The solution $\boldsymbol{x}_0^*$ to the optimization problem in Eq. (3) is now called (Mu et al., 2003, 2010) the conditional nonlinear optimal initial perturbation (CNOP-I). It has the largest nonlinear evolution at a prediction time t given the specific constraint. If the objective function is regarded as a measurement of the prediction error, the CNOP-I is the initial perturbation that results in the largest prediction error at the prediction time t. Previously, the CNOP-I approach has been used to study the predictability of ENSO events, the sensitivity analysis of the thermohaline ocean circulation, the stability of the wind-driven ocean circulation, and for defining objective observations for typhoons (Mu and Duan, 2003; Mu et al., 2004; Terwisscha van Scheltinga and Dijkstra, 2008; Mu et al., 2009).

To investigate the effects of model parameter errors on the prediction, Mu et al. (2010) extended the CNOP approach to find the optimal mode of model parameter perturbations. Suppose a parameter perturbation $\boldsymbol{p}'$ is superimposed on the model parameter $\boldsymbol{p}$, then the solution to Eq. (1) can be written as

$$\boldsymbol{X}(t) + \boldsymbol{x}_{\mathrm{p}}(t) = \boldsymbol{M}_t(\boldsymbol{p} + \boldsymbol{p}')(\boldsymbol{X}_0) \,, \tag{5}$$

where $\boldsymbol{x}_{\mathrm{p}}(t)$ denotes the departure from the reference state $\boldsymbol{X}(t)$ at the prediction time t. Generally, uncertain model parameters result from parameterizations, and their values are determined from observations. The parameter perturbations should therefore satisfy some constraint conditions. Under the given constraints, what are the parameter perturbations that cause the largest departure from the given reference state?

To address this problem, we define a nonlinear optimization problem as follows:

$$J(\boldsymbol{p}^*) = \max_{p' \in C_\sigma} J(\boldsymbol{p}') \,, \tag{6}$$

where $\boldsymbol{p}' \in C_\sigma$ denotes the parameter constraints, and C_σ often is expressed as $C_\sigma = \{\boldsymbol{p}' = (p'_1, p'_2, \cdots, p'_m) \| p'_1| \leqslant \sigma_1, |p'_2| \leqslant \sigma_2, \cdots, |p'_m| \leqslant \sigma_m\}$. The objective function $J(\boldsymbol{p}')$ is defined as

$$J(\boldsymbol{p}') = \frac{1}{2} \left\| \boldsymbol{M}_t(\boldsymbol{p}+\boldsymbol{p}')(\boldsymbol{X}_0) - \boldsymbol{M}_t(\boldsymbol{p})(\boldsymbol{X}_0) \right\|^2 . \tag{7}$$

It follows that $\boldsymbol{M}_t(\boldsymbol{p}+\boldsymbol{p}')(\boldsymbol{X}_0) - \boldsymbol{M}_t(\boldsymbol{p})(\boldsymbol{X}_0) = \boldsymbol{x}_{\rm p}(t)$. The norm in Eq. (7) is used to measure magnitudes of the departure $\boldsymbol{x}_{\rm p}(t)$, and its definition depends on the physical problem under consideration. The solution $\boldsymbol{p}^*$ to Eq. (6) was referred to as CNOP-P (Mu et al., 2010). From Eqs. (6) and (7), we can see that if the reference state $\boldsymbol{X}(t)$ is the true state, then the CNOP-P denotes the parameter perturbation that causes the largest prediction errors under the given constraint conditions. The upper bound of the prediction errors can be estimated using Eq. (6).

To obtain the CNOP-I and CNOP-P by solving the nonlinear optimization Eqs. (3) and (6) numerically, the Spectral Projected Gradient 2 (SPG2) algorithm is used. The detailed descriptions of how to derive the CNOP-I and CNOP-P using the SPG2 algorithm are shown in the Appendix A.

3. Description of the numerical ocean model

Although Qiu and Miao (2000) and Tsujino et al. (2006) suggested that baroclinic instability and mesoscale eddies play an important role in the formation of the KLM, Schmeits and Dijkstra (2001) and Pierini (2006) simulated the Kuroshio path transitions very well using a reduced-gravity shallow-water model. The latter results indicate that a reduced-gravity shallow-water model contains the essential dynamic mechanism of the Kuroshio path variations. This motivated our choice to use this model to calculate the CNOPs and address the predictability of the KLM.

The reduced-gravity shallow-water model describes the flow in a thin upper layer of the ocean superimposed on a much deeper quiescent lower layer. In this study, the governing shallow-water equations were nondimensionalized using the length scale r_0 which is radius of the earth, the mean depth of the upper layer H, a characteristic horizontal velocity scale U, an advective time scale r_0/U , and a wind-stress scale τ_0. The nondimensional equations are written as

$$\varepsilon\left(\frac{Du}{dt} - uv\tan\theta\right) - v\sin\theta = \frac{-\varepsilon F}{\cos\theta}\frac{\partial h}{\partial\phi} + E\left(\nabla^2 u - \frac{u}{\cos^2\theta} - \frac{2\sin\theta}{\cos^2\theta}\frac{\partial v}{\partial\phi}\right) + F_\phi \,, \tag{8}$$

$$\varepsilon\left(\frac{Dv}{dt} + u^2\tan\theta\right) + u\sin\theta = -\varepsilon F\frac{\partial h}{\partial\phi} + E\left(\nabla^2 v - \frac{v}{\cos^2\theta} + \frac{2\sin\theta}{\cos^2\theta}\frac{\partial u}{\partial\phi}\right) + F_\theta \,, \tag{9}$$

$$\frac{\partial h}{\partial t} + \frac{1}{\cos\theta}\left[\frac{\partial(hu)}{\partial\phi} + \frac{\partial(hv\cos\theta)}{\partial\theta}\right] = 0 \,. \tag{10}$$

In these equations u is the zonal velocity, v is the meridional velocity, h is the layer thickness, ϕ is the coordinate in the zonal direction, and θ is the coordinate in the meridional direction. The material derivative is given by

$$\frac{D}{dt} = \frac{\partial}{\partial t} + \frac{u}{\cos\theta}\frac{\partial}{\partial\phi} + v\frac{\partial}{\partial\theta} \,. \tag{11}$$

Expressions for the parameters in the equations are

$$\varepsilon = \frac{U}{2\Omega r_0}, E = \frac{A_{\rm H}}{2\Omega r_0^2}, F = \frac{g'H}{U^2} \,,$$

where Ω is the angular velocity of the earth, $A_{\rm H}$ is the lateral friction coefficient, and g' is the reduced gravity. The terms F_ϕ and F_θ in Eqs. (8) and (9) are defined as follows:

$$F_\phi = \frac{\alpha\tau_\phi}{h} - \mu u \,, \tag{12}$$

$$F_\theta = \frac{\alpha\tau_\theta}{h} - \mu v \,, \tag{13}$$

where τ_ϕ and τ_θ are the zonal component and meridional component of wind stress, respectively. In addition, $\mu = R_{\rm I}/(2\Omega)$, where $R_{\rm I}$ is the interfacial friction coefficient. The wind stress coefficient is $\alpha = \tau_0/(2\Omega\rho HU)$, where τ_0 is the amplitude of wind stress.

For the spatial differential operators in the Eqs. (8)–(10), a central finite difference discretization scheme was used on a staggered grid and the local discrete operators were defined. Subsequently, the local operators were assembled over the whole domain, forming global discrete operators (see, e.g., Dijkstra, 2005).

For the time discretization, the implicit Crank–Nicholson scheme was used to define the discrete operators. Hence, a large system of nonlinear algebraic equations had to be solved at each time step. In this study, we used the Newton–Raphson method to solve the system of the equations. It is well known that the Crank–Nicholson scheme is unconditionally stable for linear equations, and thus supports a relatively large

Table 1. The standard values of parameters in the shallow-water model.

Parameter	Value
Radius of the earth r_0	6.37×10^6 m
Scale for upper-layer thickness H	500 m
Acceleration of gravity g	9.8 m s^{-2}
Upper-layer density ρ	1023.5 kg m^{-3}
Wind stress amplitude τ_0	0.1 Pa
Lateral friction coefficient $A_{\rm H}$	450 m^2 s^{-1}
Scale for velocity U	0.1 m s^{-1}
Angular velocity of the earth Ω	7.292×10^{-5} s^{-1}
Interfacial friction coefficient $R_{\rm I}$	4.3752×10^{-8} s^{-1}
The reduced gravity g'	0.044 m s^{-2}

time step. But we should note that a time step that is too large leads to large discretization errors, limiting the convergence domain of the Newton–Raphson process (Schmeits and Dijkstra, 2001). By considering different time steps to test the model, we found that a time step of 10 days gives sufficiently accurate results.

An advantage of this implicit version of the reduced-gravity shallow-water model is that the Jacobian matrix, i.e., the tangent linear model, could be directly obtained during the implicit time stepping. In addition, the adjoint model was obtained by transposing the Jacobian matrix (see Appendix B). This contributed to the efficiency of the calculation of the CNOP-I (Terwisscha van Scheltinga and Dijkstra, 2008).

To simulate the Kuroshio path variations, the domain of integration was set as a part of the North Pacific basin (15°–55°N, 122°E–158°W). The horizontal resolution was 0.2° × 0.2°; Simonnet et al. (2003) suggested this spatial resolution to be sufficient to capture the strongly nonlinear behavior of the Kuroshio. Some studies have found that the realistic inclination of the Japanese coast is important to the simulation of the Kuroshio path (Chao and McCreary, 1982; Saiki, 1982; Pierini, 2006, 2008). Hence, we use a realistic coastline, but we used the 200-m depth contour as the continental boundary; otherwise, the modeled Kuroshio would enter the East China Sea. No-slip boundary conditions were used in the model. The model ocean was forced using the monthly averaged climatological wind stress of Hellerman and Rosenstein (1983). Standard parameter values in the model are shown in Table 1.

4. Simulated results and analysis

After 10 years of time integration, the solution of the ocean model reached a statistical steady state. The model was next integrated for an additional 20 years; the results of this 20-year integration are analyzed below.

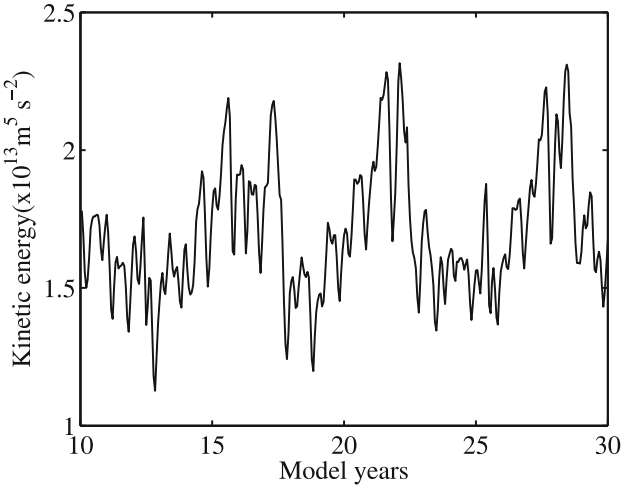

Fig. 2. Time series of the kinetic energy in the Kuroshio region south of Japan (25°–35°N, 132°–140°E).

To show the Kuroshio path variations, we used the kinetic energy in the Kuroshio region south of Japan defined by

$$E_{\rm kin}(t) = \int_\Lambda h(t)[u^2(t) + v^2(t)]dxdy, \qquad (14)$$

where Λ denotes the Kuroshio region south of Japan (25°–35°N, 132°–140°E). This kinetic energy measure was also used in Pierini (2006), who pointed out that when the kinetic energy is large, the Kuroshio is in the KLM; otherwise it is in the NLM.

The time series of the kinetic energy are plotted in Fig. 2. The figure shows that the modeled Kuroshio path variations were dominated by interannual changes and that the KLMs occurred three times in these 20 years. In model year 21, the Kuroshio shifted to the KLM, and the time of transition was a few months, which is similar to the observed transition time (Kawabe, 1995). However, the lifetime of the modeled KLM was relatively short. The reason for this may be the lack of the baroclinic instability and bottom topography in the shallow-water model, but this hypothesis needs further analysis.

To show how the modeled Kuroshio path evolved, snapshots of the upper-layer thickness field, including the KLM event of year 21–22, were shown in Fig. 3. In the reduced-gravity model, upper-layer thickness contours were regarded as approximate streamlines of the surface layer flow. As shown in Fig. 3, the sequence included the transition process of the Kuroshio path from the NLM to the KLM (and back). Figure 3a shows the Kuroshio in the typical NLM. In model year 21.33, a small meander emerged in the Kuroshio path (Fig. 3b). Over the following months, the am-

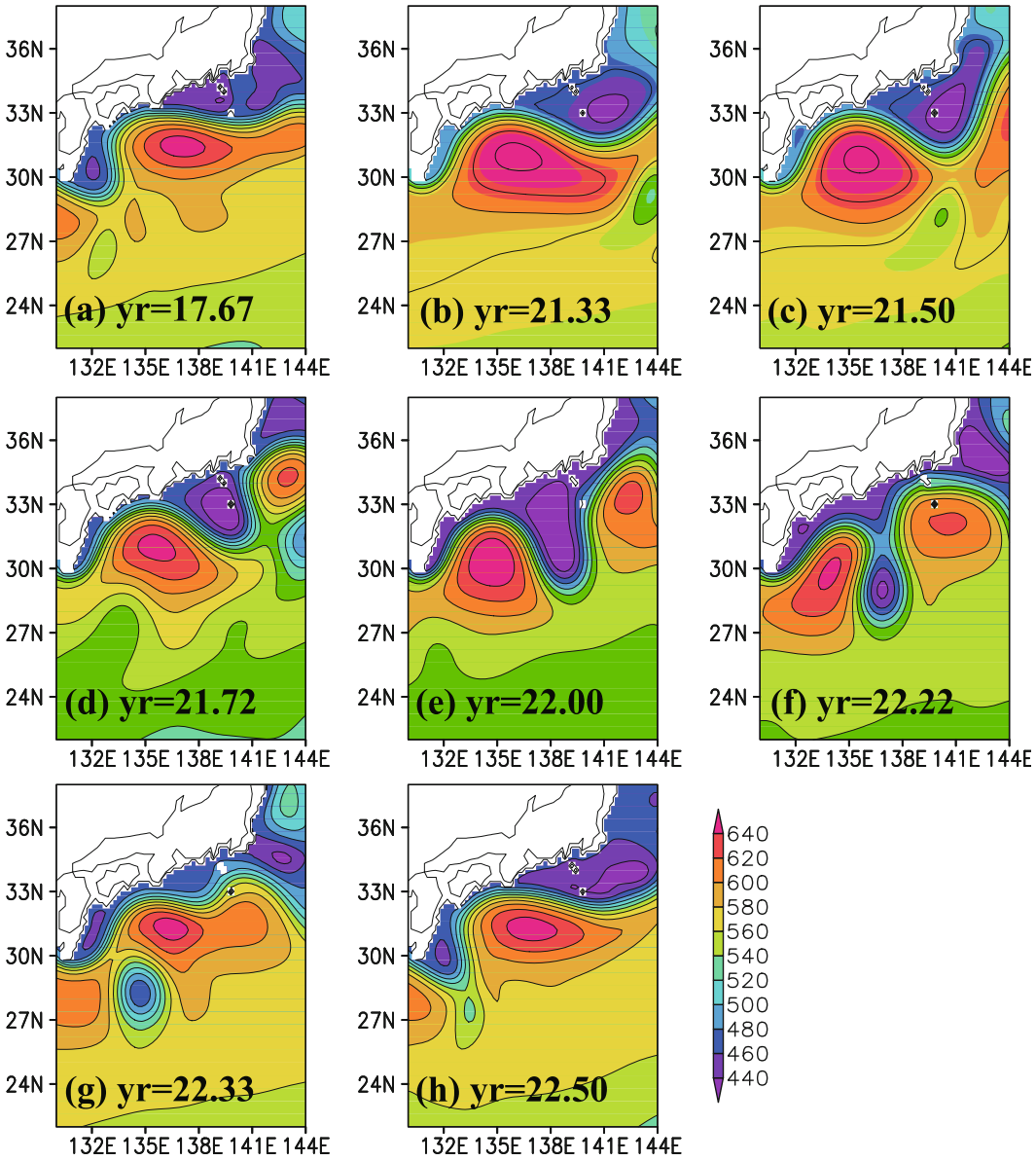

Fig. 3. Snapshots of the upper-layer thickness field including the KLM event around model year 22. Units: m.

plitude of the small meander grew steadily (Figs. 3c and 3d). The Kuroshio developed into a significant large KLM in model year 22 (Fig. 3e). The KLM was maintained for a period of time, but then an isolated cold-core eddy was shed (Fig. 3f). Figure 3g shows that the isolated cold-core eddy was detached from the KLM and propagated westward. This process was actually detected in observation data from the 1975–1979 KLM event (Nishida, 1982). Following the detachment of the cold-core eddy, the Kuroshio returned to a NLM state (Fig. 3h), similar to that shown in Fig. 3a. Notably, the results in Fig. 3 are similar to those in Fig. 9 of Qiu and Miao (2000), where a two-layer primitive-equation model was used to simulate the Kuroshio path variations.

In the following section, we focus on the formation of the KLM, i.e., the transition process from the NLM to the KLM (corresponding to the changes shown in Figs. 3b–e). The simulation results show that, although the duration of the modeled KLM is a somewhat short, the reduced-gravity shallow-water model captured the essential features of the Kuroshio path variations. In particular, the formation process of the KLM was simulated adequately, which motivated the predictability study of the KLM using the CNOP methodology with this model.

5. Impacts of the parameter errors and initial errors

In this section, we address the effect of errors in parameter values and errors in the initial condition on the prediction of the KLM by determining the CNOP-Ps and the CNOP-I. The states shown in Figs. 3b–e were the assumed reference states, and the corresponding values of parameters shown in Table 1 were regarded as reference parameter values.

To facilitate this discussion, several variables have been defined. $\boldsymbol{X}(t) = \boldsymbol{M}_t(\boldsymbol{p})(\boldsymbol{X}_0) = (u_t, v_t, h_t)^{\mathrm{T}}$ indicates the state vector at time t; $\boldsymbol{x}_0 = (u'_0, v'_0, h'_0)^{\mathrm{T}}$ represents the initial perturbation; $\boldsymbol{x}(t) = \boldsymbol{M}_t(\boldsymbol{p})(\boldsymbol{X}_0 + \boldsymbol{x}_0) - \boldsymbol{M}_t(\boldsymbol{p})(\boldsymbol{X}_0) = (u'_t, v'_t, h'_t)^{\mathrm{T}}$ is the perturbation vector at time t which results from the initial perturbation $\boldsymbol{x}_0$. Similarly, $\boldsymbol{x}_{\mathrm{p}}(t) = \boldsymbol{M}_t(\boldsymbol{p} + \boldsymbol{p}')(\boldsymbol{X}_0) - \boldsymbol{M}_t(\boldsymbol{p})(\boldsymbol{X}_0) = (u'_{t\mathrm{p}}, v'_{t\mathrm{p}}, h'_{t\mathrm{p}})^{\mathrm{T}}$ is the perturbation vector at time t caused by the model parameter perturbations $\boldsymbol{p}'$.

5.1 *Calculation of the CNOP-P*

In the shallow-water model, there are three parameters—lateral friction coefficient A_{H}, wind stress amplitude τ_0, and interfacial friction coefficient R_{I}—that are often determined empirically and have relatively large uncertainties. Hence we will examine the effects of the uncertainties in these three parameters on the prediction of the KLM.

To use the CNOP-P method, we first defined an objective function, which is a measurement of the prediction error, then we solved the maximum points of the objective function. The objective function was defined as the kinetic energy of the final perturbation in the Kuroshio region south of Japan, which can be written as

$$J(\boldsymbol{p}') = \frac{1}{2}\left\|\boldsymbol{M}_t(\boldsymbol{p}+\boldsymbol{p}')(\boldsymbol{X}_0) - \boldsymbol{M}_t(\boldsymbol{p})(\boldsymbol{X}_0)\right\|_{\mathrm{KE}} = \frac{1}{2}\left\|\boldsymbol{x}_{\mathrm{p}}(t)\right\|_{\mathrm{KE}} , \tag{15}$$

where

$$\left\|\boldsymbol{x}_{\mathrm{p}}(t)\right\|_{\mathrm{KE}} = \int_{\Lambda} (h_t + h'_{t\mathrm{p}})[(u'_{t\mathrm{p}})^2 + (v'_{t\mathrm{p}})^2]dxdy .$$

This objective function was defined according to a criterion in which the larger the difference between the forecast Kuroshio path and reference Kuroshio path is, the larger value the objective function should take, and the smaller the difference, the smaller the value of the objective function. In fact, before the objective function norm $\left\|\boldsymbol{x}_{\mathrm{p}}(t)\right\|_{\mathrm{KE}}$ was defined, we chose three different function norms to perform some experiments: (1) the difference of kinetic energies between the forecast and reference states, (2) the first-order approximation of the difference of the kinetic energies, and (3) $\left\|\boldsymbol{x}_{\mathrm{p}}(t)\right\|_{\mathrm{KE}}$. We found that $\left\|\boldsymbol{x}_{\mathrm{p}}(t)\right\|_{\mathrm{KE}}$ was able to satisfy the above criterion more than other norms. For this reason, we defined $\left\|\boldsymbol{x}_{\mathrm{p}}(t)\right\|_{\mathrm{KE}}$ as the objective function norm.

After determining the objective function, we solved the nonlinear optimization problem using [Eq. (6)] to obtain the CNOP-P numerically using the SPG2 algorithm (Birgin et al., 2000).

Four cases were considered: optimizing separately for each of the three parameters—including lateral friction coefficient A_{H} (case AH), amplitude of wind stress τ_0 (case TAU), and interfacial friction coefficient R_{I} (case RI)—and optimizing simultaneously over all three parameters (case ALL). For these four cases, the initial condition $\boldsymbol{X}_0$ in Eq. (6) was taken as the state corresponding to Fig. 3b. The optimization time was set as $t = 240$ d. The reference state corresponded to that shown in Figs. 3b–e. The reference values of the three parameters are shown in Table 1.

Next, we set the constraint condition of parameter perturbations for each case. For the amplitude of wind stress (case TAU), Kutsuwada (1982) estimated its standard deviation using the observation data and found its maximum error to be ∼0.02 Pa in the North Pacific. Hence, we set the constraint condition for case TAU as $|\tau'_0| \leqslant 0.02$ Pa. For cases RI and AH, however, there were no observations based on error estimates for R_{I} and A_{H}. In these cases, we based our estimates on the precondition that the parameter perturbation should be in an interval for which the numerical model was still able to capture the essential features of the KLM path. According to this precondition, the constraint conditions for cases RI and AH were set as $|R'_{\mathrm{I}}| \leqslant 1.4584 \times 10^{-8}$ s^{-1} and $|A'_{\mathrm{H}}| \leqslant 150$ m^2 s^{-1}, respectively. For case ALL, the condition was set as the combination of the above three conditions:

$$\begin{cases} |R'_{\mathrm{I}}| \leqslant 1.4584 \times 10^{-8} , \\ |\tau'_0| \leqslant 0.02 , \\ |A'_{\mathrm{H}}| \leqslant 150 . \end{cases} \tag{16}$$

For the precondition related to the R'_{I} and A'_{H}, we investigated the following question: How does the model respond to the parameter perturbations the are outside the bounds? We performed four experiments using different values of R'_{I} and A'_{H} to address this problem.

First, we used a value of R'_{I} larger than the upper bound of the constraint condition, and the value was set as $R'_{\mathrm{I}} = 2.1 \times 10^{-8}$, which resulted in $R_{\mathrm{I}} = 6.4752 \times 10^{-8}$. The model was integrated for 30 years, and the simulation results of the latter 20 years were used to calculate the kinetic energy using Eq. (14).

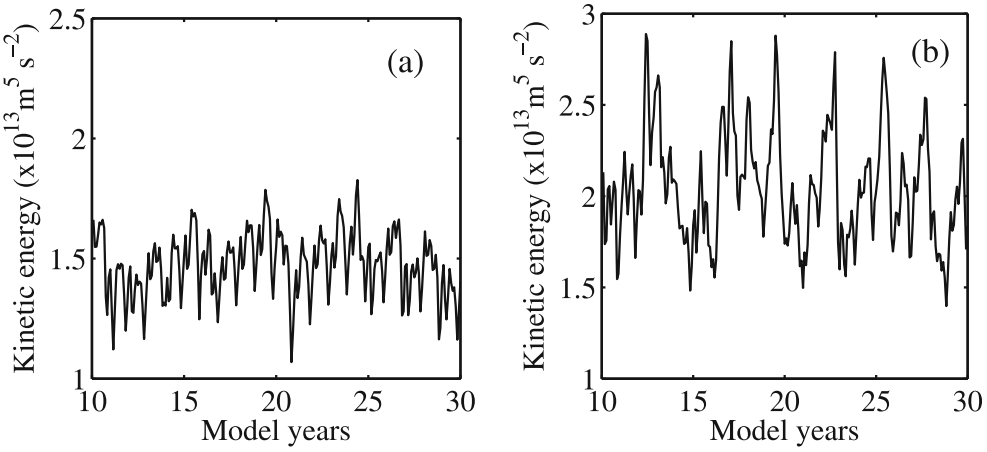

Fig. 4. Same as the Fig. 2 but for another two different values of $R_{\rm I}$, (a) $R_{\rm I} = 6.4752\times10^{-8}$, (b) $R_{\rm I} = 2.2752 \times 10^{-8}$.

Figure 4a shows the time series of the kinetic energy. We found the kinetic energy to be $\sim1.5 \times 10^{13}$ m^5 s^{-2} over the latter 20 years. In this case, the Kuroshio always had an NLM path (see Fig. 2 and Fig. 4a). That is to say, when $R_{\rm I} = 6.4752 \times 10^{-8}$, the model was not able to capture the KLM path. On the other hand, when $R'_{\rm I} = -2.1\times10^{-8}$ (namely $R_{\rm I} = 2.2752\times10^{-8}$), a similar experiment was performed, and the kinetic energy for simulation over the latter 20 years was plotted (Fig. 4b). Figure 4b shows that, although the model was able to simulate the KLM path, the path occurred too many times, i.e., the frequency of the oscillation of the Kuroshio path was higher than that of observation data. In addition, when the KLM paths occurred, all of the kinetic energies were $>2.6 \times 10^{13}$ m^5 s^{-2}, while the kinetic energy was only $\sim2.2 \times 10^{13}$ m^5 s^{-2} in Fig. 2. This means that the simulated KLM paths were too strong. Hence, when $R_{\rm I} = 2.2752 \times 10^{-8}$, the model was not able to capture a reasonable KLM path. For case AH, we performed similar computations and found that KLM paths in the model were too weak (figure not shown) when $A'_{\rm H} = 200$ (namely $A_{\rm H} = 650$). In addition, when $A'_{\rm H} = -200$ (namely $A_{\rm H} = 250$), the model became numerically unstable. Therefore, when the model parameter perturbations were outside the bounds set by the constraint conditions, the model was not able to capture reasonable KLM paths.

Next we calculated the CNOP-Ps. For each case, one CNOP-P was obtained using Eq. (6). The results are shown in Table 2. The CNOP-P for case ALL is not equal to a simple combination of the CNOP-Ps of the cases RI, TAU, and AH. Specifically, the simple combination of the CNOP-P for the parameter was -1.4584×10^{-8} s^{-1}, 0.02 Pa, -150 m^2 s^{-1}. The sign of $R'_{\rm I}$ in the combination was opposite that of the corresponding component of the CNOP-P for case ALL.

Notably, the CNOP-P for case RI caused the KLM to be overpredicted (Fig. 5, yellow line), while the corresponding component of the CNOP-P for case ALL caused the KLM to be underpredicted (Fig. 5, red line). Additionally, the CNOP-Ps for the wind stress amplitude and the lateral friction coefficient caused the KLM to be underpredicted. The error components for these two parameters in the CNOP-P for case ALL were the same as the simple combination of the CNOP-Ps for both case AH and TAU; they also caused the KLM to be underpredicted (Fig. 5, blue line). The CNOP-P for case RI demonstrated model behavior opposite that of the CNOP-Ps for case TAU and AH. Hence, if the error component for the interfacial friction coefficient in the CNOP-P for case ALL was the same as the CNOP-P for this parameter, it would have reduced the prediction error caused by the

Table 2. The CNOP-Ps for different cases.

Optimized parameter perturbation	CNOP-P	Objective function value (m s^{-2})
Interfacial friction coefficient perturbation $R'_{\rm I}$ (case RI)	-1.4584×10^{-8} s^{-1}	6.7×10^{11}
Wind stress amplitude perturbation τ'_0 (case TAU)	0.02 Pa	3.7×10^{12}
Lateral friction coefficient perturbation $A'_{\rm H}$ (case AH)	-150 m^2 s^{-1}	6.0×10^{12}
The perturbation of the three parameters (case ALL)	(1.4584×10^{-8}, 0.02, -150)	1.5×10^{13}

error components for the other two parameters in the CNOP-P for case ALL. Then the simple combination of the CNOP-P for each parameter would not have resulted in the largest prediction error. As shown in Fig. 5, the CNOP-P for case ALL caused the axis of the Kuroshio to significantly deviate from the reference axis with respect to the simple combination of the CNOP-Ps for cases RI, TAU, and AH (see the gray line and the black solid line). For this reason, the CNOP-P for case ALL, rather than the simple combination of the CNOP-P for each of three parameters, has the largest impact on the prediction of the KLM. In brief, compared to the CNOP-P for case RI, the opposite sign of the R_{I}' in the CNOP-P for case ALL achieves the purpose of CNOP-P: to maximize the measurement of the prediction error of the KLM.

5.2 *Calculation of the CNOP-I*

To determine the CNOP-I, the objective function was defined as the kinetic energy of the final perturbation in the Kuroshio region south of Japan. It is written as

$$J(\boldsymbol{x}_0) = \frac{1}{2}\left\|\boldsymbol{M}_t(\boldsymbol{p})(\boldsymbol{X}_0+\boldsymbol{x}_0) - \boldsymbol{M}_t(\boldsymbol{p})(\boldsymbol{X}_0)\right\|_{\mathrm{KE}} = \frac{1}{2}\left\|\boldsymbol{x}(t)\right\|_{\mathrm{KE}}, \tag{17}$$

where $\|\boldsymbol{x}(t)\|_{\mathrm{KE}} = \int_\Lambda (h_t + h_t')[(u_t')^2 + (v_t')^2]dxdy$, the initial state $\boldsymbol{X}_0$ is the state corresponding to the Fig. 3b. The values of the parameters were fixed (as in Table 1), and the optimal time was set as $t = 240$ d. In Eq. (3), the initial constraint norm was defined as the total energy norm of initial perturbation in the whole model domain. The total energy was defined as the sum of the kinetic and potential energy, similar to the one used by Primeau (2002). This norm was used to assess all possible causes of the error growth. Hence, the constraint condition was set as

$$\left\|\boldsymbol{x}_0\right\|_{\mathrm{TE}} = \frac{1}{2}\Big\{H\int[(u_0')^2 + (v_0')^2]dxdy + g'\int(h_0')^2 dxdy\Big\} \leqslant 3.6\times 10^{11}. \tag{18}$$

In this equation, H is the mean upper-layer depth, g' is the reduced gravity, and the magnitude of the constraint condition is 3.6×10^{11} m^5 s^{-2}. For this value, the maximal amplitudes of the perturbations of velocity of flow obtained in the initial perturbation were close to the observation error.

We again used the SPG2 algorithm (Birgin et al., 2000) to solve the optimization problem [Eq. (3)]. We found that the CNOP-I located the boundary of the initial constraint, which was consistent with the conclusion of Liu (2008). The value of the objective function at the optimum was 1.92×10^{13} m^5 s^{-2}. Figure 6a shows the distribution of the upper-layer thickness anomaly of the CNOP-I. The upper-layer thickness of the background field (Fig. 3b) was also plotted in the figure to reveal the connection between the background and the CNOP-I pattern. Figure 6b shows the evolution of the CNOP-I and the background field (Fig. 3e) at the prediction time. The perturbation at day 240 was mainly located in the target area (Fig. 6b).

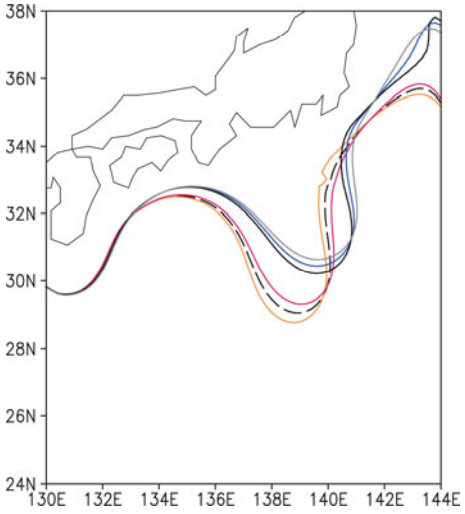

Fig. 5. The Kuroshio axes at day 240 for reference state (black dashed line), case RI (yellow line), R_{I} component of the CNOP-P for case ALL (red line), τ_0 and A_{H} components of the CNOP-P for case ALL (blue line), case ALL (gray line), and the simple combination of the CNOP-Ps of the cases RI, TAU, and AH (black solid line). The Kuroshio axis is represented as 520-m contour of the upper-layer thickness.

Figure 6a shows that the largest amplitudes of the CNOP-I were located south of Kuroshio extension and in the Kuroshio recirculation region south of Japan. This means that the perturbations located these two regions were key for the prediction of the KLM. The reason for this CNOP-I pattern may be that the Kuroshio recirculation plays an important role in the formation of the KLM. Qiu and Miao (2000) suggested that the intensification of the recirculation may result in the development of the KLM. Hence, a positive anomaly of the CNOP-I in the recirculation region had important effects on the prediction of the KLM and resulted in the large prediction error. Also, the mesoscale eddies south of the Kuroshio extension may also have been responsible for the Kuroshio path variations (Ebuchi and Hanawa, 2003), but they were not captured in this analysis. Investigating the time evolution of CNOP-I may help us to understand the physical mechanism for the formation of the KLM; however,

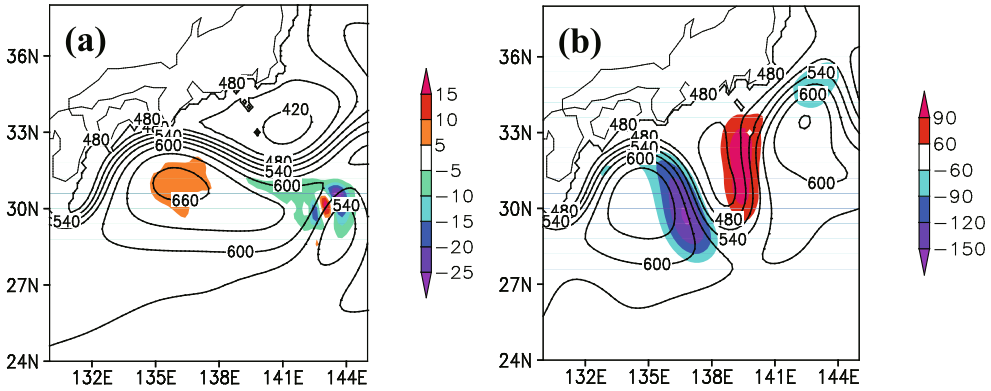

Fig. 6. Upper-layer thickness component of the perturbations (shading) and that of background field (contour) at (a) the initial time (corresponding to Fig. 3b) and (b) the prediction time $t = 240$ d (corresponding to Fig. 3e), where the perturbations at the initial time and prediction time indicate the CNOP-I and the evolution of the CNOP-I, respectively. Units: m.

this is outside the scope of this study.

5.3 *Prediction errors*

In this subsection, we compare the prediction errors caused by CNOP-I and CNOP-Ps, respectively. The value of the objective function is a measure of the prediction error. Hence, the histogram of the values of the objective function obtained during the calculation the CNOP-Ps for the different cases AH, RI, TAU, ALL, and CNOP-I were plotted (Fig. 7). The value of the objective function caused by CNOP-P for case ALL was that it was much larger than that caused by CNOP-P optimized alone for each of the three parameters. In addition, the value of the objective function caused by CNOP-I was larger than that caused by the CNOP-P for case ALL. Therefore, initial error is the most important factor in the prediction of the KLM.

Although the effects of the model parameter errors and initial error on the prediction of the KLM can be roughly seen in Fig. 7, we then focused on verifying

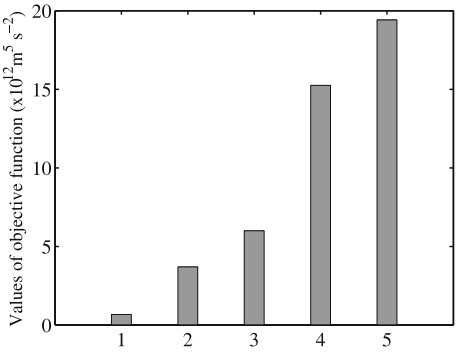

Fig. 7. The values of objective function for (1) case RI, (2) case TAU, (3) case AH, (4) case ALL, and (5) the CNOP-I.

the significance of the prediction errors and the prediction results.

First, we superimposed the CNOP-Ps (Table 2) on the reference values of the parameters, and we superimposed the CNOP-I on the initial reference state (corresponding to Fig. 3b). Then we integrated the model for 240 days. Because there were four CNOP-Ps and one CNOP-I, five forecast fields for 240 days were obtained. For each forecast field, we computed the root mean square error (RMSE; Fig. 8) with respect to the reference fields (Figs. 3b–e) of the upper-layer thickness in the Kuroshio region south of Japan (25°–35°N, 132°–140°E). The forecast skill was lower when the RMSE was larger and greater when the RMSE was smaller.

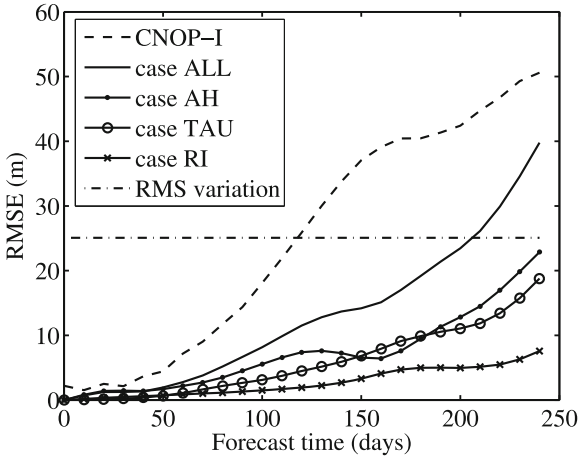

Fig. 8. Time series of root-mean-square error (RMSE) of upper-layer thickness between forecast states and reference states in the Kuroshio region south of Japan (25°–35°N, 132°–140°E).

To determine whether the prediction results were acceptable, we used a criterion based on the root mean square (RMS) variation of the upper-layer thickness in the Kuroshio region south of Japan. This criterion (shown as the dot-dashed line in Fig. 8) was used by Komori et al. (2003) and Miyazawa et al. (2005) to estimate the time limits for the prediction of the KLM. When the RMSE was larger than the RMS variation, the prediction results were unacceptable.

As shown in Fig. 8, the CNOP-P for case ALL resulted in a larger RMSE than that for each of the three parameters. In addition, the RMSE caused by the CNOP-P for case ALL was greater than the RMS variation at day 240, while the RMSE caused by the CNOP-P for each parameter was less than the RMS variation. Therefore, the CNOP-P for case ALL resulted in a significant prediction error that led to the failure of the prediction. The RMSE caused by CNOP-I was also much larger than the RMS variation. Furthermore, the RMSE caused by CNOP-I was ∼50 m at day 240, which was greater than the RMSE caused by the CNOP-P for case ALL (∼39 m). This implies that the initial error had a greater impact on the prediction of the KLM. Simultaneously, the effects of the errors of the model parameters on the prediction were not negligible because they resulted in significant prediction errors and made the forecast field unacceptable at day 240. Hence, we needed to improve the initial condition and then estimate the values of model parameters while forecasting the KLM.

Finally, to investigate the difference between the reference path and forecast paths at day 240, we plotted the Kuroshio axes from the five forecast fields (Fig. 9). The Kuroshio axis was represented as the 520-m contour of the upper-layer thickness. In Fig. 9, the forecast axis caused by CNOP-P for the case AH, RI, and TAU was not significantly different from the reference axis. However, there was a large difference between the forecast axis caused by CNOP-P for case ALL and the reference axis. The forecasted meander was much weaker than that of the reference meander. In contrast, the forecast meander caused by CNOP-I was stronger than the reference meander. These results demonstrate that the errors of the three model parameters and the initial error both had significant effects on the prediction of the KLM.

6. The sensitive analyses of the results

Previous results indicate that the prediction error caused by the CNOP-I was larger than that caused by the CNOP-Ps in the prediction of the KLM. But when calculating the CNOP-I and CNOP-Ps, we made choices about the optimization time and the final target region. Were these results sensitive to these choices?

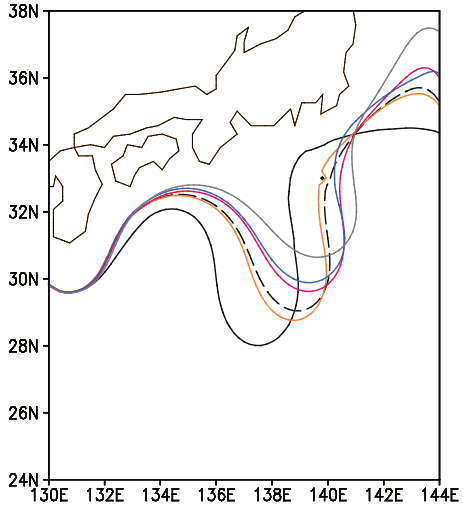

Fig. 9. The Kuroshio axes at day 240 for reference state (black dashed line), the CNOP-I (black solid line), case RI (yellow line), case TAU (red line), case AH (blue line) and case ALL (gray line). The Kuroshio axis is represented as 520-m contour of the upper-layer thickness.

To answer this question, we investigated the sensitivity of the results to the optimization time. As discussed in the section 5.1 and 5.2, the optimization time was set as $t = 240$ d. In this part of our investigation, we set another three different optimization times $t = 60$ d, t=120 d, and $t = 180$ d to calculate the CNOP-Ps and CNOP-Is. For the three different optimization times, the initial reference states were the same (see Fig. 3b). Other settings were the same as those in the sections 5.1 and 5.2. The CNOP-Ps for different optimization times are shown in Table 3. The table shows that the CNOP-Ps were different for different optimization times. Therefore, the CNOP-Ps were sensitive to the optimization time. To show the differences among the patterns of the CNOP-Is for different optimization times, the similarity coefficient was used. It is defined as

$$S = \frac{\langle \boldsymbol{e}_1, \boldsymbol{e}_2 \rangle}{\|\boldsymbol{e}_1\| \, \|\boldsymbol{e}_2\|}, \tag{19}$$

where $\|\boldsymbol{e}_i\|^2 = \langle \boldsymbol{e}_i, \boldsymbol{e}_i \rangle$, i=1,2, and the inner product is Euclidean over the whole model region. In the Eq. (19), $\boldsymbol{e}_1$ represents one of three CNOP-Is for the three optimization times t=60 d, t=120 d, and t=180 d, and $\boldsymbol{e}_2$ represents the CNOP-I for the optimization time t=240 d. Based on Eq. (19), the closer to 1 S is, the more similar $\boldsymbol{e}_1$ and $\boldsymbol{e}_2$ are. According to Eq. (19), the similarity coefficients are S=0.66, S=0.94, and S=0.93 for the optimization times t=60 d, t=120 d, and t=180 d,

Table 3. The CNOP-Ps for different optimization times.

Optimization times (d)	Case RI ($R'_{\rm I}$)	Case TAU (τ'_0)	Case AH ($A'_{\rm H}$)	Case ALL
$t = 60$	-1.4584×10^{-8}	-0.02	-150	$(-1.4584 \times 10^{-8}, 0.02, -150)$
$t = 120$	-1.4584×10^{-8}	-0.02	-150	$(1.4584 \times 10^{-8}, 0.02, -150)$
$t = 180$	-1.4584×10^{-8}	0.02	150	$(-1.4584 \times 10^{-8}, -0.02, 150)$

respectively. Therefore, some differences among the patterns of the CNOP-I for different optimization times occurred, but the differences were very small for t=120 d and t=180 d.

For each optimization time, we compared the RMSEs caused by the CNOP-Ps and CNOP-I, respectively, and the results are shown in Fig. 10. For each optimization time, the RMSE caused by the CNOP-I was greater than that result from the CNOP-Ps for different cases. This means that the initial error had a greater impact on the prediction of the KLM, which was consistent with the result presented in subsection 5.3. Hence, the conclusions obtained previously were not sensitive to the optimization times, although the CNOP-Ps were different for different optimization times and there were some differences among the CNOP-Is.

To investigate the sensitivity of the results to the final target region, we chose another two regions, Region 1: (22°–35°N, 130°–140° E) and Region 2: (28°–35°N, 135°–140°E). Because we considered the prediction of the KLM south of Japan, other regions, such as east of Taiwan or the Kuroshio extension region were not selected. For the two regions, we calculated the CNOP-Ps and the CNOP-Is, respectively. The CNOP-Ps for different regions were the same and were equal to the results shown in the Table 2. For the CNOP-Is for different target areas, we calculated the similarity coefficients using Eq. (19). In this case, the $\boldsymbol{e}_1$ in Eq. (19) represented the CNOP-I obtained for target Region 1 or Region 2, and $\boldsymbol{e}_2$ represented the CNOP-I corresponding to Fig. 6a. The coefficients were $S = 0.996$ and $S = 0.994$ for Region 1 and Region 2, respectively. Hence, the CNOP-Is for different target regions were very similar to those shown in Fig. 6a. Therefore, CNOP-P and CNOP-I were not sensitive to the choice of the final target regions in south of Japan. Similarly, the RMSEs caused by CNOP-Ps and CNOP-I for each target region were almost identical to Fig. 8 (figure not shown).

In short, the sensitivity analyses indicate that the results presented in subsection 5.3 are robust for different optimization times and final target regions.

7. Conclusions and discussion

The uncertainties in the prediction of the KLM caused by initial errors have been investigated by many researchers, but the impact of errors caused by model parameters has not. The CNOP method was capable of addressing the problems of these two aspects of the predictability study. In this study, under the assumption of ignoring other possible kinds of model errors, we investigated the effects of the errors of model

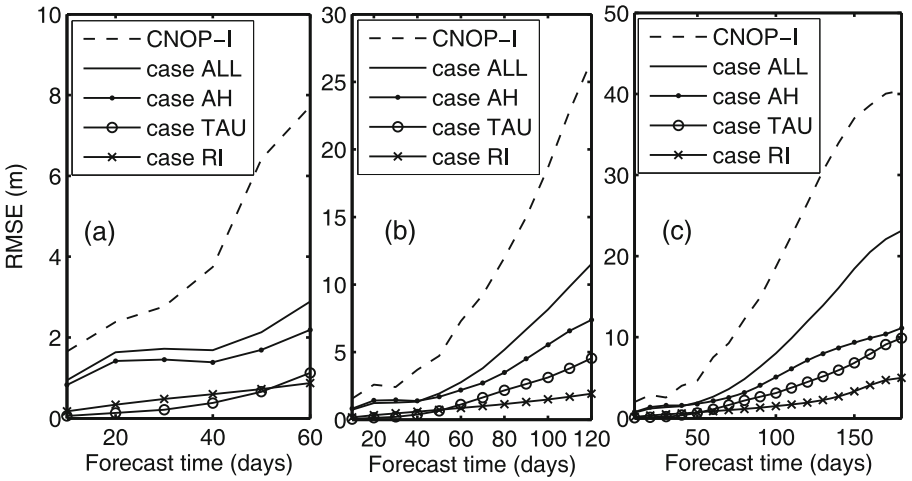

Fig. 10. Same as the Fig. 8, but for different optimization times (a) $t = 60$ d, (b) $t = 120$ d, (c) $t = 180$ d.

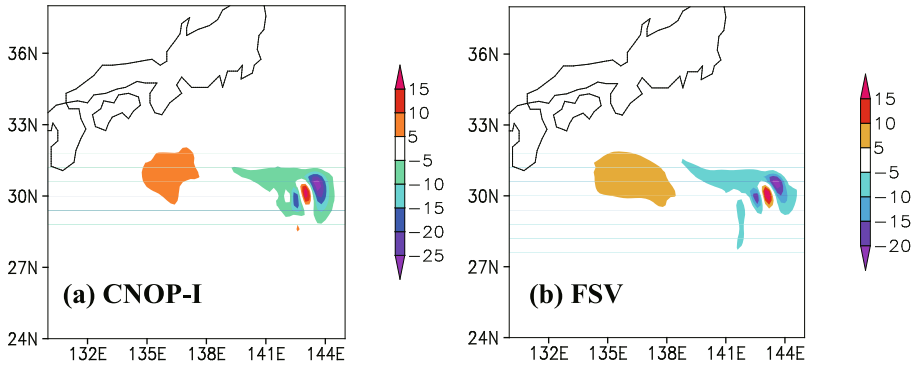

Fig. 11. Upper-layer thickness component of the (a) CNOP-I and (b) FSV. Units: m.

parameters on the prediction of the KLM using the CNOP-P method. Simultaneously, the impacts of initial error on the prediction were examined using the CNOP-I method. Both methods were applied to a reduced-gravity shallow-water model used to simulate the Kuroshio path variations. Although the model was equivalently barotropic, the results show that the model can capture the essential features of the path variations. One particular simulation was assumed as reference state, and the standard values of the parameters were regarded as reference values.

Using this model and the CNOP methodology, we examined the differences between the forecast meander states and reference states. In particular, for the model parameters, we considered four cases, including optimizing separately each of three uncertain parameters—interfacial friction coefficient, wind-stress amplitude, and lateral friction coefficient—and we optimized simultaneously for all three parameters. The results showed that the CNOP-P for all three parameters was not equal to the simple combination of the CNOP-P for each of the three parameters. For the same model and reference state, the CNOP-I was also obtained.

The impacts caused by CNOP-Ps for the different cases and CNOP-I on the prediction of the KLM were substantial. The results demonstrate that the CNOP-P optimized simultaneously for all three parameters (case ALL) resulted in a significant prediction error and made the forecast field unacceptable after 240 days. The CNOP-P optimized alone for each of three parameters, however, did not cause a large prediction error. The prediction error caused by CNOP-I was greater than that caused by the CNOP-P for case ALL. This implies that the initial condition may play a more important role in the prediction of the KLM. The role of multiple parameter uncertainties in this model, however, cannot be neglected because they also resulted in significant prediction errors. Simultaneously, the sensitive analyses indicated that these results are robust for different optimization times and final target regions. Thus, all of these results show initial error to be the dominant source of the uncertainties in the prediction of the KLM, although the model parameter errors are also important for predicting the KLM. Furthermore, to enhance the predictability of the KLM, the initial conditions should first be improved. This motivates us to develop the data assimilation system and to improve the observation parameters for Kuroshio path variations. Of course, to further reduce the prediction error, we should also estimate the values of model parameters as well as possible.

Mu et al. (2003) pointed out that the CNOP-I method is a natural generalization of the linear singular vector (SV) method into the nonlinear regime. Therefore, it was necessary to compare the CNOP-I and SV methods. Considering the first SV (FSV) to be dominant, the difference between the CNOP-I and FSV is briefly discussed here. The calculation settings for the CNOP-I and FSV are almost the same as that shown in the subsection 5.2. The only difference is that the objective function value is obtained by integrating the tangent linear model when deriving the FSV. The upper-layer thickness components of the CNOP-I and FSV are shown in Fig. 11. From the figure, we can see that the CNOP-I and FSV are similar, but there are some differences around the location (30°N, 142°E). Also, their amplitudes are different. To investigate their respective evolutions, the CNOP-I and FSV were superimposed on the initial reference state (corresponding to Fig. 3b), and then the nonlinear model was integrated for 240 days. Figure 12 shows the kinetic energy of development of the CNOP-I and FSV, demonstrating that the kinetic energy of the perturbation caused by the CNOP-I was larger than that caused by the FSV. This implies that the optimal perturbation in the nonlinear model was the CNOP-I rather than the FSV (which is optimal in the tangent linear model).

The generality of these results with respect to the

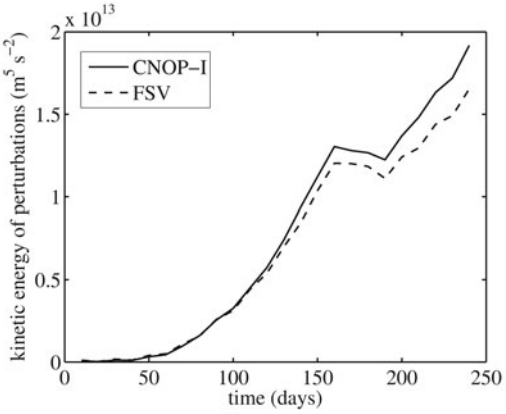

Fig. 12. The time evolution of the CNOP-I and FSV in the nonlinear model. The kinetic energy of perturbation is defined by Eq. (17) in which the time t is from day 0 to day 240.

reference state was also investigated. In fact, we calculated the CNOP-Ps and CNOP-Is for different reference states and compared their effects on the prediction of the KLM. We found there to be no qualitative differences among the results, and hence, the details are not shown in this paper. These conclusions were also obtained using a reduced-gravity shallow-water model. Whether the results are model dependent needs be further investigated, and in the near future we will use a more realistic ocean general circulation model to explore the predictability of the Kuroshio path transitions. It may be possible to better estimate the effects of the model parameter errors and initial error on the prediction of the KLM using a more realistic model.

Acknowledgements. The authors are grateful to Arjen Terwisscha van Scheltinga for providing the shallow-water model. The comments made by two anonymous reviewers helped us improve the earlier version of this manuscript. Funding was provided by the Knowledge Innovation Program of the Chinese Academy of Sciences (Grant No. KZCX2-EW-201), the Basic Research Program of Science and Technology Projects of Qingdao (Grant No. 11-1-4-95-jch), and the National Natural Science Foundation of China (Grant No. 40821092).

APPENDIX A

The Derivations of the CNOP-P and CNOP-I by the Spectral Projected Gradient 2 Algorithm

The Spectral Projected Gradient 2 algorithm (SPG2) was designed to solve the minimum problem of a nonlinear function subject to a set of constraints on the variables. The formation of the problem is written as

$$\min_{x\in\Omega} f(x)\,, \tag{A1}$$

where $f(x)$ is the objective function and $x \in \Omega$ indicates the set of constraints. For the readers' convenience, we provide the details of the SPG2 algorithm based on Birgin et al. (2000). The mathematical symbols used in following algorithm are similar to those used by Birgin et al. (2000).

Steps of algorithm SPG2 are:

Step 0: Given an integral $m \geqslant 1$; set the parameters $\alpha_{\min} > 0$ and $\alpha_{\max} > \alpha_{\min}$; set a constant parameter $\gamma \in (0,1)$ and $0 < \sigma_1 < \sigma_2 < 1$; and $\alpha_0 \in [\alpha_{\min}, \alpha_{\max}]$ is arbitrary. Given a starting iterate point x_0, if $x_0 \notin \Omega$, replace x_0 by $P_\Omega(x_0)$. The P_Ω is an projection operator and defined as $P_\Omega(x) = \arg\min_{\hat{x}\in\Omega} \|\hat{x} - x\|$. Set $k = 0$, where k indicates iteration step.

Step 1: If $\|P_\Omega[x_k - \nabla f(x_k)] - x_k\|_2 \leqslant \varepsilon$, the iteration stop and go to step 7.

Step 2: Compute $d_k = P_\Omega(x_k - \alpha_k \nabla f(x_k)) - x_k$.

Step 3: Determine λ_k using line search algorithm:

Step 3.1: Compute $f_{\max} = \max\{f(x_{j-k}) | 0 \leqslant j \leqslant \min\{k, m-1\}\}$, $x_+ = x_k + d_k$, $\delta = \langle \nabla f(x_k), d_k \rangle$, set $\lambda = 1$;

Step 3.2: If $f(x_+) \leqslant f_{\max} + \gamma\lambda\delta$, the line search stop and go to step 3.6;

Step 3.3: Compute $\lambda_{\text{temp}} = -\frac{1}{2}\lambda^2\delta / (f(x_+) - f(x_k) - \lambda\delta)$;

Step 3.4: If ($\lambda_{\text{temp}} \geqslant \sigma_1$ and $\lambda_{\text{temp}} \leqslant \sigma_2\lambda$), set $\lambda = \lambda_{\text{temp}}$, else set $\lambda = \lambda/2$;

Step 3.5: Compute $x_+ = x_k + \lambda d_k$, go to step 3.2;

Step 3.6: Set $\lambda_k = \lambda$.

Step 4: Compute $x_{k+1} = x_k + \lambda_k d_k$, $s_k = x_{k+1} - x_k$, $y_k = \nabla f(x_{k+1}) - \nabla f(x_k)$ and $\beta_k = \langle s_k, y_k \rangle$.

Step 5: If $\beta_k \leqslant 0$, set $\alpha_{k+1} = \alpha_{\max}$, else $\alpha_{k+1} = \min\{\alpha_{\max}, \max\{\alpha_{\min}, \langle s_k, s_k \rangle / \beta_k\}\}$.

Step 6: Set $k = k + 1$, go to step 1.

Step 7: Set $x_* = x_k$.

The derivations of the above algorithm have been shown by Birgin et al. (2000). In the following section, we demonstrate how to use this algorithm. In our study, the parameters in Step 0 of the algorithm are set as follows:

$$m = 10, \alpha_{\min} = 10^{-3}, \alpha_{\max} = 10^3,$$
$$\gamma = 10^{-4}, \sigma_1 = 0.1, \sigma_2 = 0.9, \alpha_0 = 1.$$

The choices of these parameters in the algorithm may be sensitive. Some choices may cause the algorithm not to reach convergence quickly. Hence, before using this algorithm, some simple tests are needed. In Step 1 of the algorithm, the parameter ε is set as $\varepsilon = 10^{-6}$.

The SPG2 algorithm is used to compute minimization problems; while CNOP-P and CNOP-I are related to the constrained maximization problems. In this case, we turn the maximization problems into the minimization problems. In particular, we rewrite the objective functions as

$$\begin{cases} J_1(\boldsymbol{p}') = -J(\boldsymbol{p}') & \text{forCNOP}-\text{P}\,, \\ J_1(\boldsymbol{x}_0) = -J(\boldsymbol{x}_0) & \text{forCNOP}-\text{I}\,, \end{cases} \tag{A2}$$

where $J(\boldsymbol{p}')$ and $J(\boldsymbol{x}_0)$ are defined by Eqs. (15) and (17), respectively. Then, we can obtain the CNOP-P and CNOP-I by solving the minimum problems of the objective function J_1 using the SPG2 algorithm.

From the algorithm SPG2, we can see that, in order to use the algorithm, three subroutines that define the objective function, the constraint conditions, and the gradient of objective function must be supplied. In our study, the objective function can be directly obtained using Eqs. (15) and (17) by the integral of the nonlinear model, and the constraint conditions are also readily derived using Eqs. (16) and (18). The most important subroutine is the definition of the gradient of objective function.

For the calculation of the CNOP-P, the gradients of objective function with respect to the perturbations of model parameters need to be supplied to the SPG2 algorithm. In this study, only three model parameters were optimized. Because the number of the parameters is very few, the derivations of the gradients become simple and need not to use the adjoint model with respect to the model parameters. The gradients can be obtained using the following finite difference approximation

$$\nabla_{\boldsymbol{p}'} J_1(\boldsymbol{p}') = \frac{\partial J_1(\boldsymbol{p}')}{\partial \boldsymbol{p}'} \approx \frac{J_1(\boldsymbol{p}'+\delta\boldsymbol{p}) - J_1(\boldsymbol{p}')}{\delta \boldsymbol{p}}\,, \tag{A3}$$

where $\delta\boldsymbol{p}$ denotes the very small perturbation.

For the calculation of the CNOP-I, however, the dimension of the initial field is 240 000—too large to directly calculate the gradient of objective function with respect to initial perturbations by the finite difference approximation. In this case, we need to derive the formula of the gradient of the objective function with respect to initial perturbations.

According to Eqs. (A2) and (17), we have

$$\begin{aligned} J_1(\boldsymbol{x}_0) &= -J(\boldsymbol{x}_0) = -\frac{1}{2}\left\|(u_t', v_t', h_t')^{\mathrm{T}}\right\|_{\mathrm{KE}} \\ &= -\frac{1}{2}\int_{\Lambda}(h_t+h_t')[(u_t')^2+(v_t')^2]dxdy \\ &\approx -\frac{1}{2}\sum\nolimits_{\Lambda}\Delta x\Delta y(h_t+h_t')[(u_t')^2+(v_t')^2]\,, \end{aligned} \tag{A4}$$

where $\sum_{\Lambda}$ denotes the summation over the region Λ.

The first-order variational of $J_1(\boldsymbol{x}_0)$ is as follows:

$$\begin{aligned} \delta J_1(\boldsymbol{x}_0) =& -\frac{1}{2}\Delta x\Delta y\Big\langle \boldsymbol{Q}\big((h_t+h_t')\cdot 2u_t', (h_t+h_t')\cdot \\ & 2v_t', (u_t')^2+(v_t')^2\big)^{\mathrm{T}}, \mathbf{M}\delta\boldsymbol{x}_0\Big\rangle \\ =& -\frac{1}{2}\Delta x\Delta y\Big\langle \mathbf{M}^{\mathrm{T}}\boldsymbol{Q}\big((h_t+h_t')\cdot 2u_t', (h_t+h_t')\cdot \\ & 2v_t', (u_t')^2+(v_t')^2\big)^{\mathrm{T}}, \delta\boldsymbol{x}_0\Big\rangle\,. \end{aligned} \tag{A5}$$

Hence, the gradient of $J_1(\boldsymbol{x}_0)$ with respect to $\boldsymbol{x}_0$ is

$$\begin{aligned} \nabla_{\boldsymbol{x}_0} J_1(\boldsymbol{x}_0) =& -\frac{1}{2}\Delta x\Delta y\mathbf{M}^{\mathrm{T}}\boldsymbol{Q}\big((h_t+h_t')\cdot 2u_t', (h_t+h_t')\cdot \\ & 2v_t', (u_t')^2+(v_t')^2\big)^{\mathrm{T}}, \end{aligned} \tag{A6}$$

where $\boldsymbol{Q}$ is a local projection operator and takes value 1(0) within (without) the region Λ, and $\mathbf{M}$ and $\mathbf{M}^{\mathrm{T}}$ indicate the tangent linear and adjoint model with respect to initial field, respectively. From Eq. (A6), we can see the adjoint model is needed when calculating the gradient of the objective function with respect to initial perturbations.

In summary, in this study the adjoint model with respect to model parameters is not needed because the number of the optimized parameters is very few. Of course, if we consider more model parameters in future, the adjoint model may be needed. For the calculation of the CNOP-I, we need the adjoint model with respect to the initial field, which is contributed to calculating the gradient of the objective function with respect to the initial perturbations.

APPENDIX B

Tangent Linear and Adjoint Models for Implicit Model

In this appendix, we demonstrate how to obtain the tangent linear and adjoint models for an implicit model. The derivations below are based on Terwisscha van Scheltinga and Dijkstra (2005).

Generally, a spatial discretization model can be symbolically written as

$$\boldsymbol{T}\frac{\partial \boldsymbol{w}}{\partial t} + \boldsymbol{L}\boldsymbol{w} + \boldsymbol{N}(\boldsymbol{w}) = \boldsymbol{F}, \tag{B1}$$

where $\boldsymbol{T}$ and $\boldsymbol{L}$ are discretized linear operators; $\boldsymbol{N}$ is a nonlinear operator, and $\boldsymbol{F}$ is the explicitly known forcing. The Crank–Nicholson scheme is used to define the time discrete operators in Eq. (B1) with a

time step Δt. Then, the implicit model can be written as

$$\frac{1}{\Delta t}\boldsymbol{T}\boldsymbol{w}_{i+1} + 0.5[\boldsymbol{L}\boldsymbol{w}_{i+1} + \boldsymbol{N}(\boldsymbol{w}_{i+1})] = \boldsymbol{G}_i, \quad \text{(B2)}$$

where

$$\boldsymbol{G}_i = \left\{\frac{1}{\Delta t}\boldsymbol{T}\boldsymbol{w}_i - 0.5[\boldsymbol{L}\boldsymbol{w}_i + \boldsymbol{N}(\boldsymbol{w}_i)]\right\} + 0.5(\boldsymbol{F}_i + \boldsymbol{F}_{i+1}) .$$

For simplicity, we denote $\boldsymbol{P}(\boldsymbol{w}_{i+1}) = \frac{1}{\Delta t}\boldsymbol{T}\boldsymbol{w}_{i+1} + 0.5[\boldsymbol{L}\boldsymbol{w}_{i+1} + \boldsymbol{N}(\boldsymbol{w}_{i+1})]$.

To solve the nonlinear system of Eq. (B2), Newton–Raphson method is used and the process of the iteration is as follows:

$$\boldsymbol{w}_{i+1,0} = \boldsymbol{w}_i , \quad \text{(B3a)}$$

$$\boldsymbol{w}_{i+1,l+1} = \boldsymbol{w}_{i+1,l} + \Delta\boldsymbol{w}_{i+1,l+1} , \quad \text{(B3b)}$$

$$\boldsymbol{J}\Delta\boldsymbol{w}_{i+1,l+1} = -\boldsymbol{P}(\boldsymbol{w}_{i+1,l}) + \boldsymbol{G}_i , \quad \text{(B3c)}$$

$$\boldsymbol{J} = \left.\frac{\partial \boldsymbol{P}}{\partial \boldsymbol{w}}\right|_{\boldsymbol{w}_{i+1,l}} = \frac{1}{\Delta t}\boldsymbol{T} + 0.5(\boldsymbol{L} + \mathbf{N}_{i+1,l}) , \quad \text{(B3d)}$$

where l denotes the iteration index, and $\mathbf{N}_{i+1,l}$ is the linearization of $\boldsymbol{N}$ around $\boldsymbol{w}_{i+1,l}$. From Eqs. (B3b) and (B3c), we can obtain the following equation,

$$\boldsymbol{w}_{i+1,l+1} = \boldsymbol{w}_{i+1,l} + \boldsymbol{J}^{-1}[\boldsymbol{G}_i - \boldsymbol{P}(\boldsymbol{w}_{i+1,l})] . \quad \text{(B4)}$$

Hence, we have

$$\begin{aligned}\delta\boldsymbol{w}_{i+1,l+1} =& \delta\boldsymbol{w}_{i+1,l} + \boldsymbol{J}^{-1}(\frac{\partial \boldsymbol{G}_i}{\partial \boldsymbol{w}_i}\delta\boldsymbol{w}_i - \boldsymbol{J}\delta\boldsymbol{w}_{i+1,l}) \\ =& \boldsymbol{J}^{-1}\big|_{\boldsymbol{w}_{i+1,l}} \frac{\partial \boldsymbol{G}_i}{\partial \boldsymbol{w}_i}\delta\boldsymbol{w}_i . \end{aligned} \quad \text{(B5)}$$

Assume that $\boldsymbol{w}_{i+1,l+1}$ is the convergence point of Newton–Raphson method, namely that $\boldsymbol{w}_{i+1,l+1}$ is the solution of the nonlinear system of Eq. (B2). In this case, according to the convergence criteria of Newton–Raphson method, $\boldsymbol{w}_{i+1,l+1}$ is very close to $\boldsymbol{w}_{i+1,l}$. Then, Eq. (B5) can be rewritten as

$$\delta\boldsymbol{w}_{i+1} = \boldsymbol{J}^{-1}\big|_{\boldsymbol{w}_{i+1}} \frac{\partial \boldsymbol{G}_i}{\partial \boldsymbol{w}_i}\delta\boldsymbol{w}_i . \quad \text{(B6)}$$

So, the tangent linear model can be explicitly written as

$$\begin{aligned}\mathbf{M} = \boldsymbol{J}^{-1}\big|_{\boldsymbol{w}_{i+1}} \frac{\partial \boldsymbol{G}_i}{\partial \boldsymbol{w}_i} =& [\frac{1}{\Delta t}\boldsymbol{T} + 0.5(\boldsymbol{L} + \mathbf{N}_{i+1})]^{-1}\times \\ & [\frac{1}{\Delta t}\boldsymbol{T} - 0.5(\boldsymbol{L} + \mathbf{N}_i)], \end{aligned} \quad \text{(B7)}$$

where $\mathbf{N}_{i+1}$ and $\mathbf{N}_i$ are the linearization of nonlinear operators $\boldsymbol{N}$ around $\boldsymbol{w}_{i+1}$ and $\boldsymbol{w}_i$, respectively. We can get the adjoint model by transposing the tangent linear model $\mathbf{M}$. Therefore, the tangent linear and adjoint models can be directly obtained during each time step.

REFERENCES

Akitomo, K., S. Masuda, and T. Awaji, 1997: Kuroshio path variation south of Japan: Stability of the paths in a multiple equilibrium regime. *J. Oceanogr.*, **53**, 129–142.

Birgin, E. G., J. M. Martinez, and M. Raydan, 2000: Nonmonotone spectral projected gradient methods on convex sets. *SIAM J. Optimiz.*, **10**, 1196–1211.

Chao, S. Y., and J. P. McCreary, 1982: A numerical study of the Kuroshio south of Japan. *J. Phys. Oceanogr.*, **12**, 679–693.

Chu, P. C., S. H. Lu., and Y. C. Chen, 1999: Two kinds of predictability problems in Lorenz system and climate models. Second Hayes Symposium on Seasonal to Interannual Climate Variability-The 1997/1998 ENSO Cycle. American Meteorological Society, 93–100.

Dijkstra, H. A., 2005: *Nonlinear Physical Oceanography: A Dynamical Systems Approach to the Large Scale Ocean Circulation and El Niño.* 2nd ed., Springer, Dordrecht, the Netherlands, 532pp.

Duan, W. S., and R. Zhang, 2010: Is model parameter error related to a significant spring predictability barrier for El Niño events? Results from a theoretical model. *Adv. Atmos. Sci.*, **27**, 1003–1013, doi: 10.1007/s00376-009-9166-4.

Ebuchi, N., and K. Hanawa, 2003: Influence of Mesoscale Eddies on Variations of the Kuroshio Path South of Japan. *J. Oceanogr.*, **59**, 25–36.

Hellerman, S., and M. Rosenstein, 1983: Normal monthly wind stress over the world ocean with error estimates. *J. Phys. Oceanogr.*, **13**, 1093–1104.

Ishikawa, Y., T. Awaji, N. Komori, and T. Toyoda, 2004: Application of sensitivity analysis using an adjoint model for short-range forecasts of the Kuroshio Path south of Japan. *J. Oceanogr.*, **60**, 293–301.

Kawabe, M., 1985: Sea level variations at the Izu Islands and typical stable paths of the Kuroshio. *J. Oceanogr. Soc. Japan*, **41**, 307–326.

Kawabe, M., 1995: Variations of current path, velocity, and volume transport of the Kuroshio in relation with the large meander. *J. Phys. Oceanogr.*, **25**, 3103–3117.

Kamachi, M., T. Kuragano, S. Sugimoto, K. Yoshita, T. Sakurai, T. Nakano, N. Usui, and F. Uboldi, 2004: Short-range prediction experiments with operational data assimilation system for the Kuroshio south of Japan. *J. Oceanogr.*, **60**, 269–282.

Komori, N., T. Awaji, Y. Ishikawa, and T. Kuragano, 2003: Short-range forecast experiments of the Kuroshio path variabilities south of Japan using TOPEX/Poseidon altimetric data. *J. Geophys. Res.*, **108**, doi: 10.1029/2001JC001282.

Kutsuwada, K., 1982: New computation of the wind stress over the North Pacific Ocean. *J. Oceanogr. Soc. Japan*, **38**, 159–171.

Latif, M., and T. P. Barnett, 1994: Causes of decadal climate variability over the North Pacific and North America. *Science*, **266**, 634–637.

Liu, Y. M., 2008: Maximum principle of conditional optimal nonlinear perturbation. *Journal of East China Normal University* (*Natural Science*), **2**, 131–134. (in Chinese)

Liu, Z. Y., 2002: A simple model study of ENSO suppression by external periodic forcing. *J. Atmos. Sci.*, **15**, 1088–1098.

Masuda, A., 1982: An interpretation of the bimodal character of the stable Kuroshio path. *Deep-sea Res.*, **29**, 471–484.

Miyazawa. Y., S. Yamane, X. Guo, and T. Yamagata, 2005: Ensemble forecast of the Kuroshio meandering. *J. Geophys. Res.*, **110**, doi: 10.1029 /2004J C002426.

Mu, M., and W. S. Duan, 2003: A new approach to studying ENSO predictability: Conditional nonlinear optimal perturbation. *Chinese Science Bulletin*, **48**, 1045–1047.

Mu, M., W. S. Duan, and B. Wang, 2003: Conditional nonlinear optimal perturbation and its applications. *Nonlinear Processes in Geophysics*, **10**, 493–501.

Mu, M., L. Sun, and H. A. Dijkstra, 2004: The sensitivity and stability of the ocean's thermocline circulation to finite amplitude freshwater perturbations. *J. Phys. Oceanogr.*, **34**, 2305–2315.

Mu, M., F. Zhou, and H. Wang, 2009: A method for identifying the sensitive areas in targeted observations for tropical cyclone prediction: Conditional nonlinear Optimal Perturbation. *Mon. Wea. Rev.*, **137**, 1623–1639.

Mu, M., W. S. Duan, Q. Wang, and R. Zhang, 2010: An extension of conditional nonlinear optimal perturbation and its applications. *Nonlinear Processes in Geophysics*, **17**, 211–220.

Nishida, H., 1982: Description of the Kuroshio meander in 1975–1980–Large meander of the Kuroshio in 1975–1980. *Report of Hydrographic Research*, **17**, 181–207.

Orrell, D., 2003: Model error and predictability over different timescales in the Lorenz'96 systems. *J. Atmos. Sci.*, **60**, 2219–2228.

Pierini, S., 2006: A Kuroshio Extension system model study: Decadal chaotic self-sustained oscillations. *J. Phys. Oceanogr.*, **36**, 1605–1625.

Pierini, S., 2008: On the crucial role of basin geometry in double-gyre models of the Kuroshio Extension. *J. Phys. Oceanogr.*, **38**, 1327–1333.

Primeau, F., 2002: Multiple equilibria and low-frequency variability of the wind-driven ocean circulation. *J. Phys. Oceanogr.*, **32**, 2236–2256.

Qiu, B., and W. Miao, 2000: Kuroshio Path variations south of Japan: Bimodality as a self-sustained internal oscillation. *J. Phys. Oceanogr.*, **30**, 2124–2137.

Saiki, M., 1982: Relation between the geostrophic flux of the Kuroshio in the eastern China Sea and its large meanders in south of Japan. *Oceanogr. Mag.*, **32**, 11–18.

Schmeits, M. J., and H. A. Dijkstra, 2001: Bimodal behavior of the Kuroshio and the Gulf Stream. *J. Phys. Oceanogr.*, **31**, 3435–3456.

Simonnet, E., M. Gill, K. Ide, R. Temam, and S. Wang, 2003: Low-frequency variability in shallow-water models of the wind-driven ocean circulation. Part 1: Steady-state solution. *J. Phys. Oceanogr.*, **33**, 712–728.

Taft, B. A., 1972: Characteristics of the flow of the Kuroshio south of Japan. *Kuroshio—Its Physical Aspects*, H. Stommel and K. Yoshida, Eds., University of Tokyo Press, 165–216.

Terwisscha van Scheltinga, A. D., and H. A. Dijkstra, 2005: Nonlinear data-assimilation using implicit models. *Nonlinear Processes in Geophysics*, **12**, 515–525.

Terwisscha van Scheltinga, A. D., and H. A. Dijkstra, 2008: Conditional nonlinear optimal perturbations of the double-gyre ocean circulation. *Nonlinear Processes in Geophysics*, **15**, 727–734.

Tsujino, H., N. Usui, and H. Nakano, 2006: Dynamics of Kuroshio path variations in a high resolution general circulation model. *J. Geophys. Res.*, **111**, doi: 10.1029/2005JC003118.

Usui, N., H. Tsujino, Y. Fujii, and M. Kamachi, 2006: Short-range prediction experiments of the kuroshio path variabilities south of Japan. *Ocean Dynamics*, **56**, 607–623.

Waseda, T., H. Mitsudera, B. Taguchi, and Y. Yoshikawa, 2002: On the eddy-Kuroshio interaction: Evolution of mesoscale eddy. *J. Geophys. Res.*, **107**, doi: 10.1029/2000JC000756.

Waseda, T., H. Mitsudera, B. Taguchi, and Y. Yoshikawa, 2003: On the eddy-Kuroshio interaction: Meander formation process. *J. Geophys. Res.*, **108**, doi: 10.1029/2002JC001583.

Yasuda, I., J. H. Yoon, and N. Suginohara, 1985: Dynamics of the Kuroshio large meander-Barotropic model. *J. Oceanogr. Soc. Japan*, **41**, 259–273.

Yu, Y. S., 2009: Studies of ENSO "Spring Predictability Barrier" problem. Ph.D. dissertation, Institute of Atmospheric Physics, Chinese Academy of Sciences, 123pp. (in Chinese)